Modelling Molecular Emitters in Organic Light Emitting Diodes with the Quantum Mechanical Bespoke Force Field

Lupeng Yang,[†] Joshua T. Horton,[‡] Michael C. Payne,[†] Thomas J. Penfold,[‡] and Daniel J. Cole[*,‡]

†*TCM Group, Cavendish Laboratory, 19 JJ Thomson Ave, Cambridge CB3 0HE, United Kingdom*

‡*School of Natural and Environmental Sciences, Newcastle University, Newcastle upon Tyne NE1 7RU, United Kingdom*

E-mail: daniel.cole@ncl.ac.uk

Abstract

Combined molecular dynamics (MD) and quantum mechanics (QM) simulation procedures have gained popularity in modelling the spectral properties of functional organic molecules. However, the potential energy surfaces used to propagate long-time scale dynamics in these simulations are typically described using general, transferable force fields designed for organic molecules in their electronic ground states. These force fields do not typically include spectroscopic data in their training, and importantly there is no general protocol for including changes in geometry or intermolecular interactions with the environment that may occur upon electronic excitation. In this work, we show that parameters tailored for thermally activated delayed fluorescence (TADF) emitters used in organic light emitting diodes (OLEDs), in both their ground and electronically excited states, can be readily derived from a small number of QM calculations using the QUBEKit (QUantum mechanical BEspoke toolKit) software, and improve the overall accuracy of these simulations.

1 Introduction

Organic light-emitting diodes (OLEDs) have emerged as a state-of-the-art technology for displays and lighting as illustrated by their presence in the majority of recent smartphone designs. However, despite this success there remains a need to improve the performance and sustainability of these devices. The key part of an OLED device is the emission layer which usually consists of small organic molecule emitters embedded within a thin film of host material. While most commercial products are based on fluorescent and phosphorescent emitters, much academic interest has shifted towards materials harnessing other mechanisms, such as thermally activated delayed fluorescence (TADF) and consequently these molecules and materials have been studied extensively both experimentally [1,2] and computationally [3–6] in recent years. Computational modelling can provide an accurate description of the singlet and triplet excited-state manifolds and explain structural and electrostatic effects on the properties of the emitting layer, which in turn can assist with designing better TADF materials.

On the atomistic scale of modelling, density functional theory (DFT) and its time-dependent variant (TD-DFT) have become the most routinely used quantum mechanical (QM) tools for calculating the ground and excited state electronic structure of TADF molecules, due to their low computational cost compared to the more accurate but much more expensive wave-function based methods. The Tamm-Danncoff approximation (TDA) and range-separated hybrid functionals are frequently employed to improve the accuracy of the calculated excited state energies. [7,8] However, most (TD-)DFT studies on emitters in the literature are performed in vacuum or with a polarisable continuum model (PCM) representing the solvent environment. [9–11] Thus, the effects of the host molecules on the emitters are rarely accounted for explicitly, despite solvation effects playing an important role in the TADF process. Indeed, it is well documented that high-performing TADF molecules require close interplay between charge transfer (CT) and locally excited (LE) states to facilitate rapid triplet harvesting. [3,12,13] A CT state usually possesses an excited state dipole moment significantly larger than its electronic ground state, while a LE state does not, and therefore

the energy gap between the CT and LE states will be heavily influenced by solvation effects. In the native amorphous organic thin film, and with analogy to the solvatochromic effect in solution, a solid state host with higher polarity can be expected to stabilise the CT state and red-shift the emission energy. However, a further complication for OLEDs is thay unlike the solution phase, the amorphous nature of the host material can produce permanent local electric fields and restrict the reorientation of the emitter. Our understanding of the complex nature of solid state solvation effects in OLEDs could be significantly enhanced by atomistic modelling.

To address this issue, electronic structure calculations are typically combined with molecular mechanics sampling of the potential energy surfaces of the host-guest system.[14,15] These combined protocols usually involve two stages: i) perform a molecular dynamics or Monte Carlo sampling with classical force fields on a combined guest-host system (which can easily comprise tens of thousands atoms or more) and ii) conduct QM calculations on snapshots taken from the MD trajectory. In the second stage, the host molecules can be treated as the MM region in QM/MM[5,16] calculations to include the electrostatic effects of the environment, whilst reducing the computational cost. With recent advances in linear-scaling density functional theory software, it is also possible to treat the entire system quantum mechanically in the evaluation of excited state properties of snapshots of the system.[17] However, in all cases, step i) above requires the use of approximate molecular mechanics force fields to sample the dynamics of the system in the condensed phase.

Notably, the force fields used in the simulations mentioned above are usually transferable force fields such as OPLS (optimised potentials for liquid simulations), GAFF (general Amber force field) and UFF (universal force field). These force fields share similar functional forms, and their parameters are usually trained to reproduce QM or experimental properties of small organic molecules. A common underlying approximation of these force fields is that their libraries of the atom, bond, angle and torsion types are transferable and can be applied to molecules outside the training set. Moreover, they are mostly designed for simulating small

molecules in a biological context. We note two major problems associated with applying these general-purpose force fields to OLED material simulations. Firstly, not all the atom, bond, angle and torsion types present in the OLED molecules are included in these force fields, in which case partial refit or parameter tweaking is required.[18] Also, since the atom types do not change upon electronic excitation, neither do the bonded parameters, limiting the ability of the force field to account for geometric changes (for example, bond elongation or torsional rotation) in the excited state. Secondly, the parameters themselves in these force fields correspond to the ground state only, whereas, in OLED research, electronic excited states (for example, low lying singlet (S_1) and triplet (T_1) states) are often just as relevant, in particular for the calculation of emission properties. While it is possible to extract force field charges from quantities such as the electronic excited state density or potential,[15] there is no guarantee that these will be compatible with the rest of the force field. This is particularly problematic for the development of Lennard-Jones parameters suitable for electronic excited states, as they are highly interdependent on the force field charges and usually rely on experimental data, such as liquid density, for their fitting.

One united atom force field has been designed specifically for OLED simulations,[19] where the training set consisted of eight organic molecules commonly used as hosts in OLED research. This force field reproduced the experimental density of the eight molecules and that of two similar molecules outside the training set. Furthermore, it achieved a six-fold speed-up in condensed phase simulation compared to AMBER by treating hydrogen atoms implicitly. However, the lack of explicit hydrogen limits its usage in hydrogen-bonding systems and the study focused on ground state properties only.

Use of a general-purpose force field introduces a mismatch between the potential energy surface (PES) sampled during MD and the ideal QM surface, thus complicating the interpretation of host-induced environmental effects in OLED materials. It has been reported in a combined MM and QM study of the structural and vibrational properties of a light harvesting apocarotenoid, peridinin, that standard transferable force fields perform poorly in

reproducing bond lengths, electronic excitations, spectral densities and vibrational features, in comparison with specifically tuned force fields.[20] The necessity of developing molecule- and state-specific force fields for modelling TADF molecules has been highlighted in a recent perspective paper.[21] Force fields derived from QM calculations specifically for a molecule of interest represent a fundamentally different approach, which can address the aforementioned need. Various methods to generate *ab initio* force fields from QM exist in the literature, for example, by fitting force field parameters to reproduce QM energies and forces for a set of configurations,[22–25] or by breaking down the QM interaction energy with intermolecular perturbation theory.[26–28] However, most of these methods employ more complex functional forms compared to the transferable force fields, which increases their computational expense and reduces their compatibility with popular MD packages.

Here, we employ the recently developed QUantum mechanical BEspoke (QUBE) force field, which can be generated using QUBEKit,[29] a toolkit designed for automating the determination of molecule-specific all-atom force field parameters from QM. The QUBE force field employs the same functional form as OPLS, and the derivation of all but the torsional parameters requires only a single QM optimisation of the molecule under study. In brief, QUBEKit derives the bond and angle parameters of a given molecule from the Hessian matrix of the QM optimised structure using the modified Seminario method,[30] the charges and Lennard-Jones parameters from an atoms-in-molecule analysis of the electron density, and the torsional parameters by performing relaxed QM scans around the chosen dihedrals. QUBEKit has been tested on the liquid properties of a set of 109 organic molecules and the resulting force field demonstrated comparable or better accuracy in predicting liquid densities, heats of vaporisation, and free energies of hydration, compared to OPLS and GAFF. In addition, normal mode vibrational frequencies calculated from the QUBE force field show good agreement with QM frequencies. This advantage can be particularly valuable for modelling TADF molecules, where low-frequency torsional modes are thought to play an important role in assisting the emission process[3] and enhancing coupling between excited

states[13] via conformational fluctuations, and high frequency modes can strongly influence the shapes of the ground and excited state potential energy surfaces.

The solid state solvation effect of a TADF emitter, PTZ-DBTO2, in hosts with different polarity has been previously studied in detail using a combined MD and TD-DFT approach.[15] PTZ-DBTO2 consists of a phenothiazine donor (coloured in grey) and a dibenzothiophene-S,S-dioxide acceptor (coloured in black) as shown in Figure 1**a**. Both X-ray data and DFT calculations show that the donor and acceptor arrangement can exist in two forms, referred to as axial and equatorial, with respect to the N–S axis and plane of the phenyl rings.[31] The two forms are sometimes also referred as perpendicular and co-planar in the literature. The equatorial configuration is preferable for TADF due to the near perpendicular arrangement between the donor and the acceptor for this isomer. QM calculations reveal that the HOMO and LUMO orbitals reside mainly on the donor and the acceptor, respectively, with little overlap. The first singlet excitation of PTZ-DBTO2, which is dominated by the HOMO–LUMO transition, is known to possess a strong charge transfer character.[32] The other two molecules shown in Figure 1, CBP and PYD2 are commonly used host materials in the OLED community. In this work, we model the excited state properties of PTZ-DBTO2 in these solid state hosts using the QUBE force field. We show that this molecule-specific force field notably allows us to model both geometric and environmental contributions to the Stoke's shift of PTZ-DBTO2, which was missing from previous studies which used transferable MM force fields.[15]

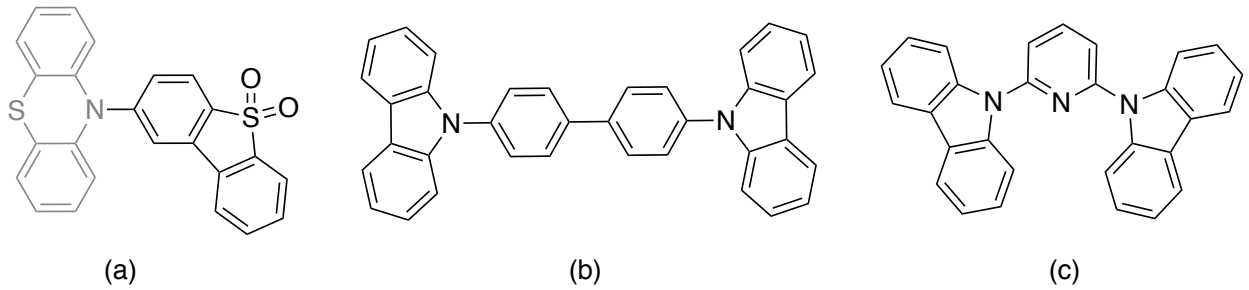

Figure 1: molecular structures of (a) phenothiazine-dibenzothiophene-S,S-dioxide (PTZ-DBTO2), (b) 4,4-N,N-dicarbazole-biphenyl (CBP) and (c) 2,6-dicarbazolo-1,5-pyridine (PYD2).

2 Computational Methods

2.1 Parameterisation of Hosts and Guest

QUBEKit was employed to derive force field parameters for the S_0 and S_1 states of the guest molecule, PTZ-DBTO2, and the S_0 states of the host molecules, CBP and PYD2. Molecular structures are shown in Figure 1. The QUBE force field takes the same functional form as OPLS:

$$\begin{aligned} U = & \sum_{Bonds} \frac{k_r}{2}(r - r_0)^2 + \sum_{Angles} \frac{k_\theta}{2}(\theta - \theta_0)^2 \\ & + \sum_{Dihedrals} \left[\frac{V_1}{2}(1 + \cos(\phi)) + \frac{V_2}{2}(1 - \cos(2\phi)) + \frac{V_3}{2}(1 + \cos(3\phi)) + \frac{V_4}{2}(1 - \cos(4\phi)) \right] \\ & + \sum_{Pairs} \frac{q_i q_j}{r_{ij}} + \left(\frac{A_{ij}}{r_{ij}^{12}} - \frac{B_{ij}}{r_{ij}^{6}} \right) \end{aligned} \quad (1)$$

QUBEKit parameterises the following terms in equation 1: equilibrium bond lengths (r_0) and angles (θ_0) and their corresponding force constants k_r and k_θ, coefficients V_1, V_2, V_3 and V_4 for the cosine series describing the dihedral interactions, atomic charges q_i, and the 12-6 Lennard-Jones potential coefficients A_{ij} and B_{ij}.[29] For the latter, OPLS mixing rules are used to determine Lennard-Jones coefficients for pairs of atoms i and j. All QM calculations in this study were performed with the Gaussian09 package.[33] Geometry optimisations were performed in vacuum using DFT for S_0 states and TD-DFT for S_1 states with the M06-2X functional and def2-SVP basis set. In contrast to literature suggestions, the Tamm–Dancoff approximation (TDA) was not used here for the S_1 state of PTZ-DBTO2 because it failed to produce an optimised structure with no imaginary frequencies. Bond and angle parameters were calculated from the Hessian matrix of the optimised structures using the modified Seminario method.[30] Single point calculations were subsequently performed using the optimised structures in an implicit solvent. The Guassian09 default PCM using the integral equation formalism[34] was employed with the static dielectric constant, ϵ, set to 4 to account for

induction in an effective manner.[35] Atomic partial charges were computed using density derived electrostatic and chemical (DDEC) atoms-in-molecule partitioning of the total electron density, using the DDEC3 method in the Chargemol program.[36,37] Lennard-Jones parameters were derived from the resulting atomic electron densities using the Tkatchenko-Scheffler method, as previously described.[29,35]

Dihedral scans were performed for all freely rotatable torsion angles in the three molecules. The dihedral parameters V_1 to V_4 were fit by minimising the difference between MM and QM constrained one-dimensional torsional scans.[29] As in our previous work, torsion scans for the host molecules were performed using our interface between QUBEKit and the Gaussian09[33] and BOSS[38] software packages. However, due to the complex nature of the potential energy surface of the guest molecule, all dihedral scans for PTZ-DBT02 were performed using a new interface with TorsionDrive.[39] In contrast to a regular linear scan, TorsionDrive uses a wave-front propagation method which tends to produce a smoother and more symmetric potential energy surface. This is particularly important for ground state PTZ-DBTO2 because the central nitrogen atom exhibits a change in pyrimidalisation during the scan, which can lead to hysteresis in the torsion scans. Interfaces between TorsionDrive and the Gaussian09 and QUBEKit codes have been developed for this task, and can be accessed on GitHub (https://github.com/lpwgroup/torsiondrive). All remaining force field parameters, namely rigid torsion coefficients and those for toluene, were taken from OPLS-AA. No off-centre charges were used in this work.[29]

2.2 MD sampling

Final QUBE force fields were output as xml files, and all MD simulations were performed using OpenMM[20] on GPUs with python scripts (**Supporting Data**). A single PTZ-DBTO2 molecule was solvated in a 5x5x5 nm^3 box of each host using the *insert-molecules* function of the GROMACS package.[40] Periodic boundary conditions (PME for non-bonded forces) and the NPT ensemble (achieved with the Langevin integrator and the Monte Carlo barostat)

were used for all MD runs.

The system was equilibrated at 300 K before gradually being heated up to 1000 K over 0.7 ns. Another equilibration for a period of time between 1 and 1.6 ns was carried out at 1000 K, after which the system was cooled down to 300 K over a 0.7 ns period. Finally, a 2 ns production run was performed at 300 K. The heating process raised the temperature of the system above its melting point, thus allowing free movement of all molecules and faster equilibration. The heating process was omitted for simulations in toluene since it is a liquid at room temperature.

The QUBE force field fitted to the S_0 state of PTZ-DBTO2 was used up to this point, and the same process was repeated twenty times. Ground state properties were calculated using the snapshots at the end of each S_0 state simulation cycle. The force field parameters for PTZ-DBTO2 in each of the twenty snapshots were then instantaneously swapped to the S_1 state and MD sampling was resumed for a further 100 ns. All excited state properties were calculated with snapshots extracted from the final 100 ns MD runs.

Note the heating and cooling procedure for the S_0 state sampling in solid hosts is intended to simulate the production process of OLEDs, for example, vacuum thermal evaporation or spin-coating. The S_1 state sampling performed at 300 K is intended to simulate a system under rapid photo-excitation, for example, by a laser beam.

2.3 QM calculations

Single point TD-DFT calculations were performed using the Gaussian09 package[33] on snapshots from the MD ensembles to calculate the 20 lowest energy electronic excited states. Both pure TD-DFT and TDA were used but the differences between the two methods will be shown later to be small (< 0.05 eV). The emitter was treated fully quantum mechanically, whereas host molecules within 8 Å of the guest were included as point charges with the charges being the same as the ones used in the MD simulations. Basis sets and exchange correlation functionals were kept consistent with the force field parameterisation step. Example

QM input files are provided in the **Supporting Data**.

3 Results and Discussion

3.1 Force Field Validation

The quality of the parameterised QUBE force field is first examined by comparing quantities including normal mode frequencies, dipole moments, optimised structures and potential energy surfaces around key dihedrals, with QM data. Figure 2 shows the vibrational normal mode frequencies of PTZ-DBTO2 in the S_0 and S_1 states from QM optimisations plotted against frequencies obtained following MM optimisation using the QUBE force field. The mean unsigned errors (MUE) between MM and QM calculated frequencies are 25.7 and 25.2 cm^{-1} (4.0 and 3.5%) for S_0 and S_1 states, respectively. The agreement, here, with QM is actually slightly better than the expected accuracy (6.3%) of the modified Seminario method, which has been benchmarked previously for small organic molecules in the ground state.[29,30]

Table 1 compares the dipole moments calculated from the DDEC atoms-in-molecule point charges, that are used to build the QUBE force field, with the underlying QM data. Recall that the atoms-in-molecule charges are computed from the QM electron density in implicit solvent (PCM), which tends to increase molecular polarization compared to vacuum.[35] Table 1 shows that the dipole moments computed using the DDEC point charges are in excellent agreement with the QM dipoles in PCM. In cases where there is strong anisotropy in the partitioned atomic electron densities, we would not necessarily expect such good agreement between the point charge model and QM, but off-centre charges can be used to account for this.[29] However, given the agreement between QM and QUBE dipole moments, we judged that these were not required here.

The QM optimised structures of PTZ-DBTO2 in the S_0 and S_1 states are shown in Figure 3. To allow a comparison of the QM optimised geometry with that of the QUBE

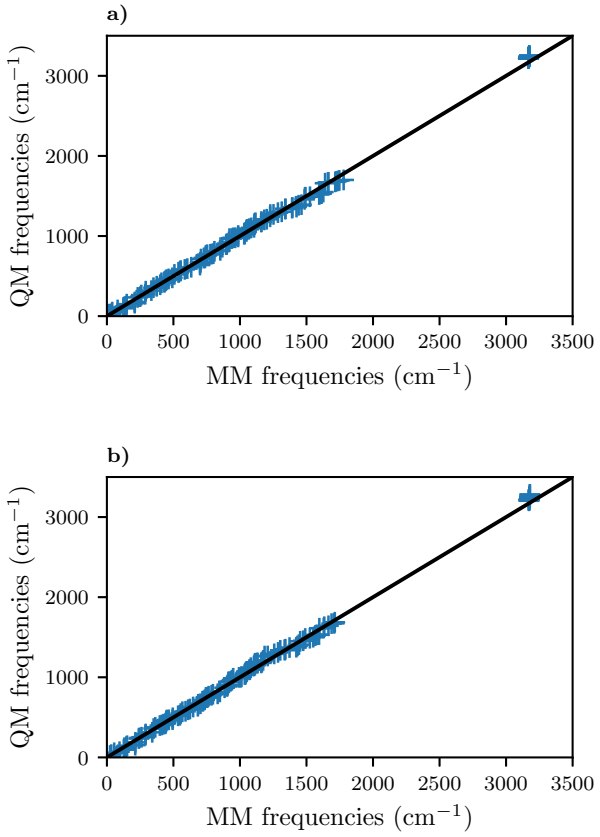

Figure 2: Comparison between normal mode frequencies calculated using QM and the QUBE force field for **a)** the ground state S_0 and **b)** the first electronic excited state S_1 of PTZ-DBTO2. Black lines have a gradient of 1 and thus represent perfect agreement.

Table 1: Comparison between dipole moments (Debye) calculated from QM and QUBE force field charges. The QM PCM values are extracted from single point calculations of the optimised structures in PCM with dielectric constant of 4.

	PTZ-DBTO2 S_0	PTZ-DBTO2 S_1	CBP S_0	PYD2 S_0
QM vacuum (D)	5.67	19.13	0.07	2.57
QM PCM (D)	5.68	22.09	0.07	3.21
QUBE (D)	5.72	22.50	0.05	3.01

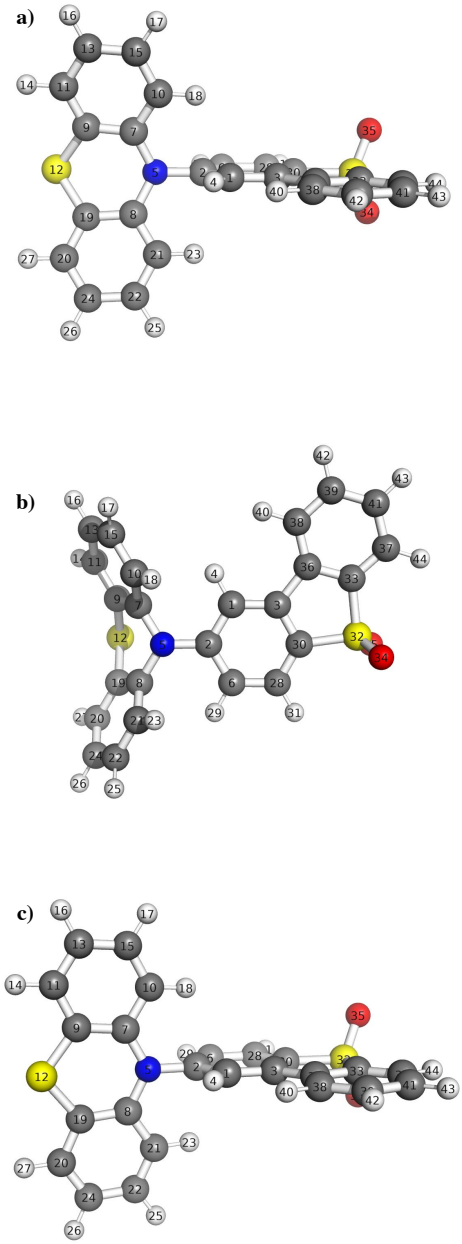

Figure 3: QM optimised structures of PTZ-DBTO2: **a)** S_0 equatorial from unconstrained DFT optimisation, **b)** S_0 axial from DFT torsion scan and **c)** S_1 equatorial from unconstrained TD-DFT optimisation.

force field, a selection of bonds, angles and dihedrals (mainly involving heavy atoms) are listed in Table 2. Note that, in QUBE, although the MM equilibrium bond lengths and angles are set equal to the optimised QM values, they may change during optimisation due to, for example, steric effects from Lennard-Jones interactions. Most of the bond lengths agree well with differences usually less than 0.005 Å, except those involving the nitrogen atom, where the errors are around 0.02–0.03 Å. Note that the expected 0.02 Å elongation of the N(5)-C(2) bond upon electronic excitation from S_0 to S_1 is reproduced by QUBE. For the angles, the maximum difference is 3.7° for C(9)-S(12)-C(19) in the S_0 state. The biggest discrepancy between the optimised QM and QUBE structures occurs in the dihedral angle of C(7)-N(5)-C(2)-C(1) in the S_0 state. By examining the improper torsion C(7)-N(5)-C(2)-C(8) in the optimised QM structures, it is clear that the nitrogen atom in the S_1 state is in a trigonal planar configuration, whereas in the S_0 state, it exhibits a pyramidal shape. That is, the donor part of the guest molecule roughly remains in the same plane in the S_1 state, but exhibits a bend in the S_0 state (Figure 3). This in turn decreases the value of the dihedral angle C(7)-N(5)-C(2)-C(1) from 90° to 80° (Figure 3(a)). However, the MM optimised structure of the S_0 state failed to capture the pyramidal configuration of the nitrogen atom since no improper torsions were re-parameterised in this work. As a consequence, the potential energy surface around the dihedral C(7)-N(5)-C(2)-C(8) is harder to fit in the S_0 state than the S_1 state. Despite the change in pyrimidalisation, in both S_0 and S_1 QM optimised structures, the plane containing C(1), C(3), C(6) and C(28) is perpendicular to the plane containing C(7), C(8), C(9) and C(19), which is in good agreement with the QUBE optimised structures.

The full potential energy surfaces around the central torsion C(7)-N(5)-C(2)-C(1) of PTZ-DBTO2 in the S_0 and S_1 states are shown in Figure 4. There are two distinct minima for the S_0 state that are very close in energy, an axial configuration (Figure 3**b**) where the dihedral angle of C(7)-N(5)-C(2)-C(1) is around 15°, and the equatorial configuration discussed above (Figure 3**a**) where the dihedral angle is around 80°. The x-ray crystal structure (CCDC-

Table 2: Comparison of a selection of geometry elements between QM and MM. Two atoms bond length (in Å), three atoms angle (in degrees) and four atoms dihedral angle (in degrees). The atom numbers are displayed in Figure 3.

Geometry	S_0 QM	S_0 MM	S_1 QM	S_1 MM
S(32)=O(35)	1.452	1.449	1.461	1.460
O(34)=S(32)=O(35)	119.9	120.2	117.1	117.2
S(32)-C(30)	1.792	1.789	1.771	1.779
S(32)-C(33)	1.791	1.787	1.779	1.775
C(30)-S(32)-C(33)	91.7	90.7	91.8	91.0
S(12)-C(9)	1.769	1.769	1.730	1.728
C(9)-S(12)-C(19)	99.1	102.8	103.1	105.3
N(5)-C(2)	1.428	1.443	1.448	1.468
N(5)-C(7)	1.415	1.441	1.382	1.411
C(7)-N(5)-C(8)	121.8	124.8	124.9	126.6
C(7)-N(5)-C(2)-C(1)	80.1	90.8	90.6	89.6
C(7)-N(5)-C(2)-C(8)	160.2	179.2	178.7	179.2

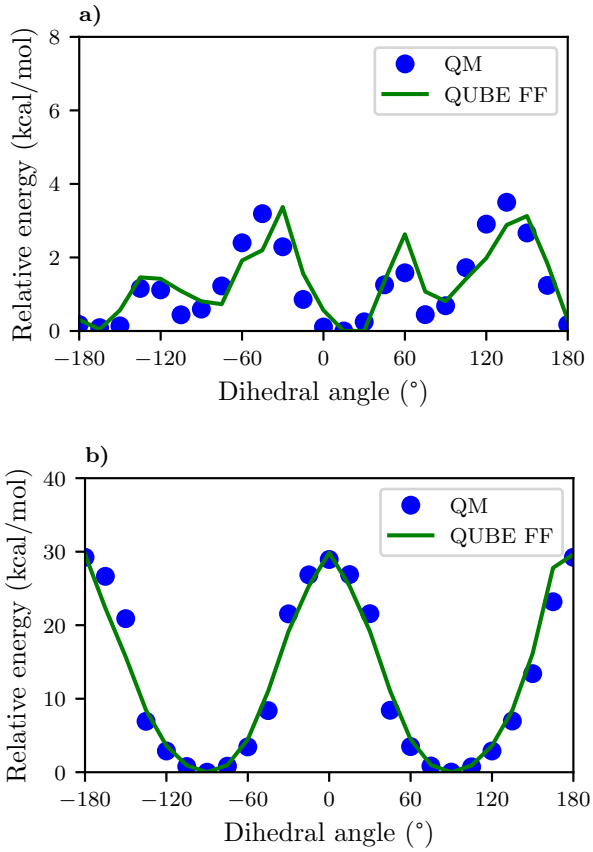

Figure 4: The QM and final QUBE potential energy surfaces around the central flexible dihedral (C(7)-N(5)-C(2)-C(1)) of PTZ-DBTO2 in **a)** S_0 and **b)** S_1 states.

1040892) of PTZ-DBTO2 is found to be in the axial conformation,[41] though this may be influenced by crystal packing effects. The improper torsion of C(7)-N(5)-C(2)-C(8) for the two configurations are -153.3 and 163.5, respectively, which indicates that there is a flip of N with respect to the plane containing C(2), C(7) and C(8). The coupling between the proper and improper torsion degrees of freedom in this molecule leads to a rather complex potential energy surface, for which a simple dihedral energy potential of 4-body sinusoidal functions (as used in QUBE) is challenging to fit. Nevertheless, using the interface between QUBEKit and TorsionDrive, the full scan shown in Figure 4 is in reasonably good agreement with QM. In contrast, the S_1 state has only one well-defined minimum at around 90°, which corresponds to the equatorial conformation (Figure 3**c**). More importantly, the improper torsion C(7)-N(5)-C(2)-C(8) remains close to 180° during the scan and, hence, the potential energy surface obtained from the QUBE scan for S_1 is in good agreement with QM.

Finally, we highlight the non-bonded parameters for atoms whose partial charges change by more than 0.05 e between the S_0 and S_1 states of the guest molecule (Table 3). The parameters of C(13) and O(34) are the same as of C(24) and O(35) due to symmetry. During the transition from S_0 to S_1, the donor loses 0.81 e in total according to the summed DDEC charges, of which N(5) and S(12) alone contribute 0.45 e. This total charge transfer is close to the assumption that one full electron is transferred between the donor and the acceptor.[15] Also of note are the changes in the σ parameters of the LJ potential, which is one of the key advantages of bespoke force field design. Using a standard, transferable force field, the LJ parameters are determined by the atom type, which does not change upon electronic excitation. However, if we examine N(5), for example, we can see that the electron density on this atom decreases in the S_1 state (atomic charge more positive). This leads to a corresponding reduction in the LJ σ parameter (from 0.312 to 0.294 nm), which is intuitive given the decrease in electron density on this atom. Thus, by allowing both bonded and non-bonded force parameters to respond to the electronic state of the molecule, we should be able to model both structural and host-guest contributions to the emission properties of

PTZ-DBTO2.

Table 3: Comparison of QUBE force field parameters for the S_0 and S_1 states of PTZ-DBTO2. Note that A and B Lennard-Jones parameters are related to ϵ (the depth of the L-J potential well) and σ (the separation at which the L-J potential is zero) via $A = 4\epsilon\sigma^{12}$ and $B = 4\epsilon\sigma^{6}$. Only σ is reported here since ϵ does change in QUBE, by construction.

Atom	PTZ-DBTO2 S_0		PTZ-DBTO2 S_1	
	charge(e)	σ(nm)	charge(e)	σ(nm)
C(2)	0.231	0.341	0.135	0.347
N(5)	-0.211	0.312	0.020	0.294
C(6)	-0.192	0.357	-0.370	0.375
S(12)	-0.086	0.349	0.134	0.340
C(13)	-0.137	0.356	-0.054	0.349
C(24)	-0.137	0.356	-0.054	0.349
O(34)	-0.650	0.293	0.703	0.296
O(35)	-0.650	0.293	0.703	0.296

3.2 Molecular Dynamics Simulations

Examples of the time dependence of the central (C(7)-N(5)-C(2)-C(1)) dihedral angle of PTZ-DBTO2 during S_0 dynamics of PTZ-DBTO2, in toluene and the two solid state hosts, are shown in Figure 5 (first 5 ns of each simulation). Recall that twenty such runs were performed in each host to sample available conformations. For both CBP and PYD2, it is clear that PTZ-DBTO2 can transform between the equatorial and axial conformations during the heating and cooling process. However, once the sampling enters the final 2 ns of equilibration at 300 K, the configuration is locked due to the rigidity of the solid state host. In the examples shown, the guest can be locked in either the axial (Figure 5**b**) or equatorial (Figure 5**c**) conformations.

On the other hand, the guest molecule is a lot more flexible in liquid toluene at 300 K. In the S_0 sampling cycle shown in Figure 5**a**, PTZ-DBTO2 started in the equatorial configuration, switched into the axial configuration at around 1.8 ns, and transformed back into the equatorial state at 3 ns. This distribution can be explained by the low energy barrier between the two conformers, which is only about 2 kcal/mol (0.087 eV) in vacuum.

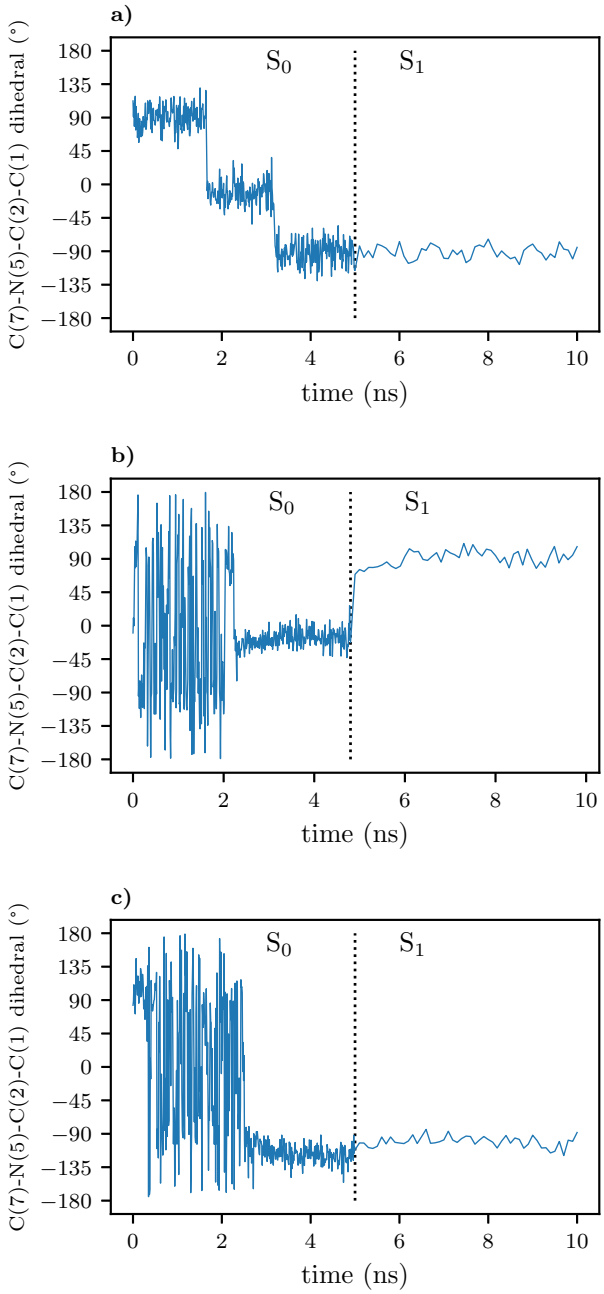

Figure 5: Time dependence of the central dihedral angle of PTZ-DBTO2 during MD sampling in **a)** toluene, **b)** CBP and **c)** PYD2. Each of the plots corresponds to one of the twenty sampling runs. For the first 5 ns (dashed line), the emitter is modelled in the S_0 state, before switching to the S_1 state force field. Note that simulations in the solid state hosts include an initial heating phase to equilibrate the system.

Table 4: Relative populations of equatorial and axial conformations of PTZ-DBTO2 at the end of S_0 sampling for PTZ-DBTO2 in each host.

host	equatorial	axial
toluene	85%	15%
CBP	55%	45%
PYD2	75%	25%

The relative populations of the two conformations in each of the hosts after 5 ns of each of the twenty MD runs are summarised in Table 4. Thus, although the two conformations of PTZ-DBTO2 are very similar in energy in vacuum, transfer to either solution or the solid state seems to promote a higher population of the equatorial structure.

Figure 5 also shows examples of the conformational behaviour of the emitters after switching to the S_1 state force field at 5 ns. It is noteworthy, as can be seen in Figure 5**b**, that the axial conformation in the CBP solid state host immediately switches to the equatorial (while the conformation in the other two simulations is relatively unchanged). Indeed, in all of our simulations the axial configurations flipped into the equatorial conformations within a few nanoseconds, even in the rigid, solid state environment of CBP and PYD2. This is expected given the very high energy of the axial conformation in the S_1 state (Figure 4**b**).

3.3 Absorption and Emission Energetics

Table 5: Absorption (S_1^{abs}) and emission (S_1^{emi}) energies, and Stoke's shifts ($S_1^{abs} - S_1^{emi}$), of PTZ-DBTO2 in different environments calculated from TD-DFT + TDA. Values in parentheses are computed using pure TD-DFT. Data from this work (QUBE) are compared with transferable force field approaches from the literature (Standard).[15]

	S_1^{abs} (eV)		S_1^{emi} (eV)		Stoke's shift (eV)		
	QUBE	Standard	QUBE	Standard	QUBE	Standard	μ (D)
In vacuo	3.65 (3.63)	3.65	2.65 (2.64)	2.65	1.00	1.00	-
In CBP	3.63 (3.57)	3.49	2.75 (2.74)	2.84	0.88	0.65	0.07
In toluene	3.42 (3.39)	3.43	2.11 (2.11)	2.77	1.31	0.66	0.43
In PYD2	3.55 (3.50)	3.33	2.51 (2.50)	3.36	1.04	-0.03	2.57

Absorption and emission energies of PTZ-DBTO2 in the different environments are averaged over twenty MD runs and the results are summarised in Table 5. The *in vacuo* vertical

excitation energies are calculated using the optimised geometries shown in Figure 3**a** and 3**c**. A separate single point calculation on the axial conformation of PTZ-DBTO2 in the S_0 state (Figure 3**b**) gives an absorption energy of 4.26 eV, suggesting that the absorption energy has a strong dependence on the angle between the donor and the acceptor. We note that our S_1 structure is optimised with pure TD-DFT, in contrast to TD-DFT+TDA in previous work.[15] However, the computed emission energies are the same, which suggests that there is little difference between the geometries optimised using the two methods. Moreover, the vertical excitation energies calculated from pure TD-DFT are only a few meV lower than the TDA values for all solvents (Table 5), and so we focus only on the TD-DFT+TDA data here.

The experimental absorption and emission energies of PTZ-DBTO2 in toluene are 3.75 and 2.05 eV, respectively, with a corresponding Stoke's shift of 1.7 eV.[32] Thus, the emission energy (2.11 eV) obtained in this work is in excellent agreement with the experimental value, and the value of the Stoke's shift (1.31 eV) is also closer to the experiment, compared to previous work using standard, transferable force fields (0.66 eV).[15] Since the parameters of toluene should be relatively accurate in all transferable force fields, the difference here is mainly due to the inclusion of molecule-specific bond, angle, dihedral and non-bonded parameters corresponding to the S_1 state of PTZ-DBTO2 in the QUBE force field. In particular, by allowing the bonded parameters of the force field (such as the N(5)-C(2) bond length) to adjust according to the electronic state of the molecule, we potentially capture both the geometric and host-guest contributions to the Stoke's shift. In contrast, previous work has used standard, transferable force field parameters and atom typing,[15] where the S_0 and S_1 states shared the same bond, angle, dihedral and Lennard-Jones parameters, an approach which neglects, in particular, the structural changes to the molecule upon electronic excitation.

We note that the Stoke's shift in toluene for the current work is still 0.4 eV smaller than the experimental value. The discrepancy could be caused by the fact that the solvent is

only included as point charges in the QM calculation. Thus, only approximate electrostatic interactions between PTZ-DBTO2 and its environment are accounted for, neglecting other factors such as dipole-induced dipole interactions. Additionally, we showed in the previous section that there is rapid exchange between the axial and equatorial conformations of the molecule in the S_0 state on this time scale. A slightly higher proportion of the axial conformation would be expected to give a higher absorption energy and, hence, an increased computed Stoke's shift.

For PTZ-DBTO2 in PYD2, a Stoke's shift of 1.04 eV is reported here, greater than that of CBP, which agrees with the general trend of solvatochromism, that is, the Stoke's shift increases as the solvent polarity increases. This is again in contrast with previous work,[15] which showed no Stoke's shift at all, where the authors argue that this is due to the rigidity of PYD2 which provides a tightly packed molecular environment and hence hinders reorientation after excitation. The authors referred to an experimental study on the photophysics of another TADF molecule, 10-phenyl-10H-spiro[acridine-9,90-fluorene]-2',7'-dicarbonitrile (ACRF), in different host matrices to support their argument.[42] The experimental work demonstrated that while embedded in PYD2, the photoluminescence (PL) spectrum of ARCF exhibited weaker blue-shift at millisecond time scales compared to other more flexible and equally polar hosts. However, it is important to point out that the same PL spectra also showed a moderate initial red-shift ($\sim$ 0.3 eV) just after photo-excitation. Note that ARCF has a smaller dipole moment (1.47 and 14.1 D for ground and excited states, respectively) than PTZ-DBTO2. We believe the difference between this work and previous work[15] comes from the use of molecule-specific force fields parameterised specifically for both the hosts and the guest. Although we observe some suppression of the Stoke's shift in the solid state (compared to in toluene), the shifts measured are similar to those observed in vacuum which points to some allowed geometric relaxation of the molecule in the excited state.

Figure 6 plots the time dependence of the S_1 energies in different environments. As

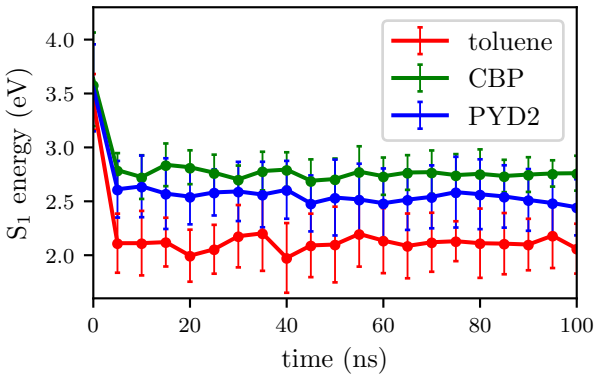

Figure 6: The time dependence of S_1 energies of PTZ-DBTO2 in different environments, averaged over twenty MD runs. At 0 ns, the emitter is in the S_0 state, after which the emitters are excited to S_1. No significant difference between pure TD-DFT (dots) and TD-DFT + TDA (solid lines) are observed.

demonstrated earlier, in Table 5, energies calculated using pure TD-DFT and TD-DFT+TDA show no significant difference. Furthermore, the results shown in Figure 6 agrees with previous work[15] that emission energies are stable after $\sim$ 50 ns, especially for the solid hosts PYD2 and CBP, since the reorientation of the hosts are restricted on this time scale.

The time dependence of the S_1 energy and the S_1-T_1 energy gap with and without background point charges representing the solvent are shown in Figure 7. Figure 7**a** shows that without the background point charges, PTZ-DBTO2 has similar S_1 energies in all hosts, which indicates that different environments do not alter the structure of PTZ-DBTO2 significantly differently. When the point charges are included, toluene lowers the S_1 energy most significantly. This is expected since, in the liquid state, solvent molecules can more easily re-orientate and align their dipoles with the emitter. These data are in qualitative agreement with previous discussion of the origin of the Stoke's shift in toluene,[15] with here $\sim$ 0.7 eV coming from interactions with the solvent (Figure 7) and the remaining $\sim$ 0.6 eV coming from structural changes in the emitter. Of course, in the current study, both effects are extracted from a single simulation, explicitly including the environmental and temperature effects, due to the use of separate QUBE force fields for the ground and excited states of the emitter. As discussed above, PYD2 leads to a slightly stronger red-shift than CBP

due to its larger dipole moment. However, the shift is much smaller than in toluene due to the more restricted solid environment.

In contrast to the results for the S_1 energy, the influence of solvent on the S_1-T_1 gap is much smaller, less than 0.1 eV. Still, lowering the S_1-T_1 gap facilities the reverse inter-system crossing process, thus enhancing TADF. Moreover, the solvent effect shown is in contrast to previous work,[15] where the environment showed no impact on the S_1-T_1 energy gap. This difference is assigned to an improved description of the excited state structure and increased CT character of the excited state in the present work.

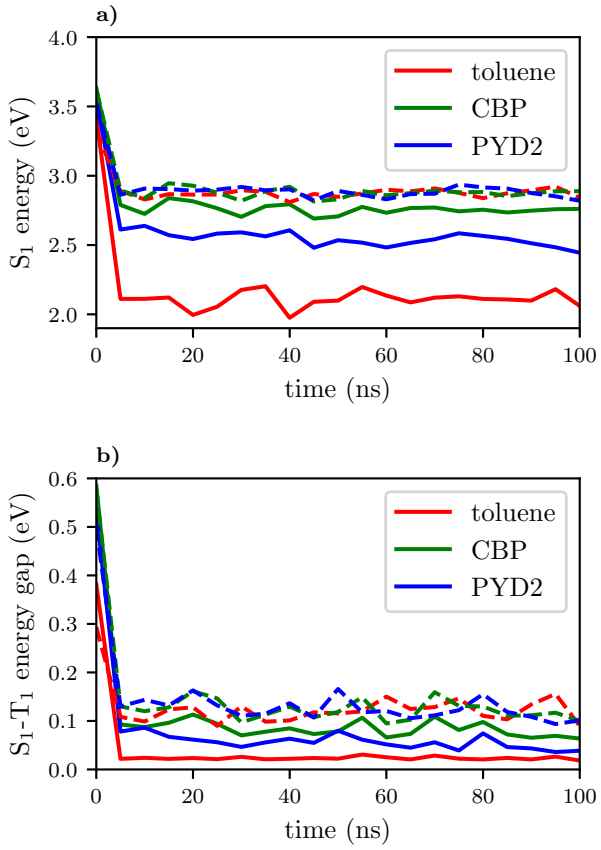

Figure 7: The time dependence of **a)** S_1 energy and **b)** S_1-T_1 energy gap with (solid lines) and without (dashed lines) background point charges representing the environment.

4 Conclusions

In the present work, we apply a quantum mechanical bespoke force field to the modelling of a molecular emitter of importance to OLED design. QUBE force field parameters are obtained for the S_0 and S_1 states of the emitter PTZ-DBTO2, and the electronic ground states of the solid state hosts, CBP and PYD2. The QUBE force field parameters show good agreement with QM data in terms of dipole moments, normal mode frequencies and potential energy surfaces along key torsion angles. The parameterised force field is then used for MD sampling of the emitter in the condensed phase, after which TD-DFT calculations are performed on snapshots to obtain absorption and emission energies. The energetics and Stoke's shift show a better agreement with experiments for PTZ-DBTO2 in toluene than previous work,[15] where transferable GAFF force field parameters are employed. Moreover, previous work did not recover any Stoke's shift for the emitter in PYD2, which appears to contrast with experiment.[42] With the QUBE force field, the missing Stoke's shift is calculated as 1.04 eV, which is greater than that of a non-polar solid host, CBP.

It is worth emphasising some of the key advantages in using the QUBE force field for this task compared to available, transferable counterparts. Firstly, by deriving bond, angle, dihedral, charge and Lennard-Jones parameters directly from a small number of QM calculations, we are able to determine molecule-specific force field parameters at a relatively low computational cost (with the torsion scan being the most time consuming part). Importantly, this gives access not only to molecule-specific, but also electronic excited state-specific, parameters if the appropriate QM electron density, Hessian matrix and torsion scans are used. In contrast, standard force fields rely heavily on parameter fits to experimental data (such as liquid densities and heats of vapourisation) and parameter assignment through atom typing, neither of which are appropriate for molecules in their excited states. Furthermore, QUBE force field parameterisation may be carried out at the same level of theory as subsequent QM post-processing calculations, which reduces mismatch between the two energy surfaces. For example, an inappropriate assigned equilibrium bond length during MD runs may strongly

affect the relative QM energies between ground and excited states in post-processing.

On the other hand, some areas for improvement in the approach used are highlighted by this study. The changes in nitrogen pyrimidalisation, which lead to the complex potential energy surface around the central dihedral angle in the S_0 state of PTZ-DBTO2, suggest that improvements could be made by including improper torsion parameterisation,[43] either through analysis of the Hessian matrix or explicit torsion scans. Although normal mode frequencies are in very good agreement with QM calculations here, it is known that further improvements are possible by including more complex force field functional forms, including couplings between torsion and other internal coordinates,[44] which might be particularly important for spectroscopic calculations. A fourth host Bis(2-(diphenylphosphino)phenyl)ether oxide (DPEPO), which was studied in previous work,[15] was not included here because QUBEKit lacks key parameters for phosphorus (in particular, the free atom radius used to derive Lennard-Jones parameters[35]). However, it will be possible to extend the number of elements included in QUBEKit in future. Finally, it should be emphasised that alternative approaches for atomistic modelling based on machine learning of the quantum potential energy surface are approaching the speeds required for these simulations,[45,46] and could readily be extended to electronic excited states. However, extension of these potentials to the condensed phase (for example, modelling long-ranged interactions) is still an open research question. The simplicity and low cost of these bespoke force field models for organic electronics, automated by the QUBEKit software, open up this field for improved design of functional materials by routinely including host-guest interactions.

Acknowledgement

The authors are grateful to Lee-Ping Wang (UC Davis) for help in implementing the TorsionDrive interface. We acknowledge financial support from a Trinity-Barlow scholarship (LY), a UKRI Future Leaders Fellowship grant MR/T019654/1 (DJC) and the EPSRC, grants

EP/R010153/1, EP/P012388/1, EP/N028511/1 and EP/R021503/1. This work also used resources provided by the Cambridge Service for Data Driven Discovery (CSD3) operated by the University of Cambridge Research Computing Service (www.csd3.cam.ac.uk), provided by Dell EMC and Intel using Tier-2 funding from the EPSRC (capital grant EP/P020259/1), and DiRAC funding from the Science and Technology Facilities Council (www.dirac.ac.uk).

Supporting Information Available

Parameterised QUBE force fields (in xml format) of PTZ-DBTO2, CBP and PYD2, PDB files of boxes of solid hosts containing the guest molecule, and sample input scripts for OpenMM and Gaussian09 are provided on the following GitHub repository: **to add**.

References

(1) Dias, F. B.; Penfold, T. J.; Monkman, A. P. Photophysics of thermally activated delayed fluorescence molecules. *Methods Appl. Fluoresc.* **2017**, *5*, 012001.

(2) Wong, M. Y.; Zysman-Colman, E. Purely Organic Thermally Activated Delayed Fluorescence Materials for Organic Light-Emitting Diodes. *Adv. Mater.* **2017**, *29*.

(3) Gibson, J.; Monkman, A. P.; Penfold, T. J. The Importance of Vibronic Coupling for Efficient Reverse Intersystem Crossing in Thermally Activated Delayed Fluorescence Molecules. *ChemPhysChem* **2016**, 2956–2961.

(4) Penfold, T. J.; Dias, F. B.; Monkman, A. P. The theory of thermally activated delayed fluorescence for organic light emitting diodes. *Chem. Commun.* **2018**, *54*, 3926–3935.

(5) de Silva, P.; Van Voorhis, T. QM/MM Study of Static and Dynamic Energetic Disorder in the Emission Layer of an Organic Light-Emitting Diode. *J. Phys. Chem. Lett.* **2018**, *9*, 1329–1334.

(6) Chen, X. K.; Zhang, S. F.; Fan, J. X.; Ren, A. M. Nature of highly efficient thermally activated delayed fluorescence in organic light-emitting diode emitters: Nonadiabatic effect between excited states. *J. Phys. Chem. C* **2015**, *119*, 9728–9733.

(7) Penfold, T. J. On predicting the excited-state properties of thermally activated delayed fluorescence emitters. *J. Phys. Chem. C* **2015**, *119*, 13535–13544.

(8) Eng, J.; Laidlaw, B. A.; Penfold, T. J. On the geometry dependence of tuned-range separated hybrid functionals. *J. Comput. Chem.* **2019**, *40*, 2191–2199.

(9) Sun, H.; Zhong, C.; Brédas, J. L. Reliable Prediction with Tuned Range-Separated Functionals of the Singlet-Triplet Gap in Organic Emitters for Thermally Activated Delayed Fluorescence. *J. Chem. Theory Comput.* **2015**, *11*, 3851–3858.

(10) Samanta, P. K.; Kim, D.; Coropceanu, V.; Brédas, J. L. Up-Conversion Intersystem Crossing Rates in Organic Emitters for Thermally Activated Delayed Fluorescence: Impact of the Nature of Singlet vs Triplet Excited States. *J. Am. Chem. Soc.* **2017**, *139*, 4042–4051.

(11) Sun, H.; Hu, Z.; Zhong, C.; Chen, X.; Sun, Z.; Brédas, J. L. Impact of Dielectric Constant on the Singlet-Triplet Gap in Thermally Activated Delayed Fluorescence Materials. *J. Phys. Chem. Lett.* **2017**, *8*, 2393–2398.

(12) Etherington, M. K.; Gibson, J.; Higginbotham, H. F.; Penfold, T. J.; Monkman, A. P. Revealing the spin-vibronic coupling mechanism of thermally activated delayed fluorescence. *Nat. Commun.* **2016**, *7*, 1–7.

(13) Penfold, T. J.; Gindensperger, E.; Daniel, C.; Marian, C. M. Spin-Vibronic Mechanism for Intersystem Crossing. *Chem. Rev.* **2018**, *118*, 6975–7025.

(14) Duan, Y.-C.; Gao, Y.; Geng, Y.; Wu, Y.; Shan, G.-G.; Zhao, L.; Zhang, M.; Su, Z.-M. Towards red-light o -carborane derivatives with both aggregation induced emission

and thermally activated delayed fluorescence combining quantum chemistry calculation with molecular dynamics simulation. *J. Mater. Chem. C* **2019**, *7*, 2699–2709.

(15) Northey, T.; Stacey, J. E.; Penfold, T. J. The Role of Solid State Solvation on the Charge Transfer State of a Thermally Activated Delayed Fluorescence Emitter. *J. Mater. Chem. C* **2017**, *5*, 11001–11009.

(16) Fan, J.; Lin, L.; Wang, C. K. Excited state properties of non-doped thermally activated delayed fluorescence emitters with aggregation-induced emission: A QM/MM study. *J. Mater. Chem. C* **2017**, *5*, 8390–8399.

(17) Zuehlsdorff, T. J.; Haynes, P. D.; Hanke, F.; Payne, M. C.; Hine, N. D. M. Solvent Effects on Electronic Excitations of an Organic Chromophore. *J. Chem. Theory Comput.* **2016**, *12*, 1853–1861.

(18) Hu, T.; Han, G.; Tu, Z.; Duan, R.; Yi, Y. Origin of High Efficiencies for Thermally Activated Delayed Fluorescence Organic Light-Emitting Diodes: Atomistic Insight into Molecular Orientation and Torsional Disorder. *J. Phys. Chem. C* **2018**, *122*, 27191–27197.

(19) Moral, M.; Son, W. J.; Sancho-García, J. C.; Olivier, Y.; Muccioli, L. Cost-Effective Force Field Tailored for Solid-Phase Simulations of OLED Materials. *J. Chem. Theory Comput.* **2015**, *11*, 3383–3392.

(20) Andreussi, O.; Prandi, I. G.; Campetella, M.; Prampolini, G.; Mennucci, B. Classical Force Fields Tailored for QM Applications: Is It Really a Feasible Strategy? *J. Chem. Theory Comput.* **2017**, *13*, 4636–4648.

(21) Olivier, Y.; Sancho-Garcia, J. C.; Muccioli, L.; D'Avino, G.; Beljonne, D. Computational Design of Thermally Activated Delayed Fluorescence Materials: The Challenges Ahead. *J. Phys. Chem. Lett.* **2018**, *9*, 6149–6163.

(22) Prampolini, G.; Livotto, P. R.; Cacelli, I. Accuracy of quantum mechanically derived force-fields parameterized from dispersion-corrected DFT data: The benzene dimer as a prototype for aromatic interactions. *J. Chem. Theory Comput.* **2015**, *11*, 5182–5196.

(23) Greff Da Silveira, L.; Jacobs, M.; Prampolini, G.; Livotto, P. R.; Cacelli, I. Development and Validation of Quantum Mechanically Derived Force-Fields: Thermodynamic, Structural, and Vibrational Properties of Aromatic Heterocycles. *J. Chem. Theory Comput.* **2018**, *14*, 4884–4900.

(24) Cacelli, I.; Cinacchi, G.; Prampolini, G.; Tani, A. Computer simulation of solid and liquid benzene with an atomistic interaction potential derived from ab initio calculations. *J. Am. Chem. Soc.* **2004**, *126*, 14278–14286.

(25) Waldher, B.; Kuta, J.; Chen, S.; Henson, N.; Clark, A. E. ForceFit: A code to fit classical force fields to quantum mechanical potential energy surfaces. *J. Comput. Chem.* **2010**, *32*, NA–NA.

(26) Xu, P.; Guidez, E. B.; Bertoni, C.; Gordon, M. S. Perspective: Ab initio force field methods derived from quantum mechanics. *J. Chem. Phys.* **2018**, *148*.

(27) Van Vleet, M. J.; Misquitta, A. J.; Stone, A. J.; Schmidt, J. R. Beyond Born-Mayer: Improved Models for Short-Range Repulsion in ab Initio Force Fields. *J. Chem. Theory Comput.* **2016**, *12*, 3851–3870.

(28) McDaniel, J. G.; Schmidt, J. R. Physically-motivated force fields from symmetry-adapted perturbation theory. *J. Phys. Chem. A* **2013**, *117*, 2053–2066.

(29) Horton, J. T.; Allen, A. E.; Dodda, L. S.; Cole, D. J. QUBEKit: Automating the Derivation of Force Field Parameters from Quantum Mechanics. *J. Chem. Inf. Model.* **2019**, *59*, 1366–1381.

(30) Allen, A. E. A.; Payne, M. C.; Cole, D. J. Harmonic Force Constants for Molecular Mechanics Force Fields via Hessian Matrix Projection. *J. Chem. Theory Comput.* **2018**, *14*, 274–281.

(31) Etherington, M. K.; Franchello, F.; Gibson, J.; Northey, T.; Santos, J.; Ward, J. S.; Higginbotham, H. F.; Data, P.; Kurowska, A.; Dos Santos, P. L.; Graves, D. R.; Batsanov, A. S.; DIas, F. B.; Bryce, M. R.; Penfold, T. J.; Monkman, A. P. Regio-And conformational isomerization critical to design of efficient thermally-activated delayed fluorescence emitters. *Nat. Commun.* **2017**, *8*, 1–11.

(32) Nobuyasu, R. S.; Ren, Z.; Griffiths, G. C.; Batsanov, A. S.; Data, P.; Yan, S.; Monkman, A. P.; Bryce, M. R.; Dias, F. B. Rational Design of TADF Polymers Using a Donor-Acceptor Monomer with Enhanced TADF Efficiency Induced by the Energy Alignment of Charge Transfer and Local Triplet Excited States. *Adv. Opt. Mater.* **2016**, *4*, 597–607.

(33) Frisch, M. J.; Trucks, G. W.; Schlegel, H. B.; Scuseria, G. E.; Robb, M. A.; Cheeseman, J. R.; Scalmani, G.; Barone, V.; Mennucci, B.; Petersson, G. A.; Nakatsuji, H.; Caricato, M.; Li, X.; Hratchian, H. P.; Izmaylov, A. F.; Bloino, J.; Zheng, G.; Sonnenberg, J. L.; Hada, M.; Ehara, M.; Toyota, K.; Fukuda, R.; Hasegawa, J.; Ishida, M.; Nakajima, T.; Honda, Y.; Kitao, O.; Nakai, H.; Vreven, T.; Montgomery, J. A., Jr.; Peralta, J. E.; Ogliaro, F.; Bearpark, M.; Heyd, J. J.; Brothers, E.; Kudin, K. N.; Staroverov, V. N.; Kobayashi, R.; Normand, J.; Raghavachari, K.; Rendell, A.; Burant, J. C.; Iyengar, S. S.; Tomasi, J.; Cossi, M.; Rega, N.; Millam, J. M.; Klene, M.; Knox, J. E.; Cross, J. B.; Bakken, V.; Adamo, C.; Jaramillo, J.; Gomperts, R.; Stratmann, R. E.; Yazyev, O.; Austin, A. J.; Cammi, R.; Pomelli, C.; Ochterski, J. W.; Martin, R. L.; Morokuma, K.; Zakrzewski, V. G.; Voth, G. A.; Salvador, P.; Dannenberg, J. J.; Dapprich, S.; Daniels, A. D.; Farkas, O.; Foresman, J. B.; Ortiz, J. V.;

Cioslowski, J.; Fox, D. J. Gaussian09 Revision E.01. Gaussian Inc. Wallingford CT 2009.

(34) Tomasi, J.; Mennucci, B.; Cammi, R. Quantum mechanical continuum solvation models. *Chem. Rev.* **2005**, *105*, 2999–3093.

(35) Cole, D. J.; Vilseck, J. Z.; Tirado-Rives, J.; Payne, M. C.; Jorgensen, W. L. Biomolecular Force Field Parameterization via Atoms-in-Molecule Electron Density Partitioning. *J. Chem. Theory Comput.* **2016**, *12*, 2312–2323.

(36) Manz, T. A.; Limas, N. G. Introducing DDEC6 atomic population analysis: Part 1. Charge partitioning theory and methodology. *RSC Adv.* **2016**, *6*, 47771–47801.

(37) Limas, N. G.; Manz, T. A. Introducing DDEC6 atomic population analysis: Part 2. Computed results for a wide range of periodic and nonperiodic materials. *RSC Adv.* **2016**, *6*, 45727–45747.

(38) Jorgensen, W. L.; Tirado-Rives, J. Molecular modeling of organic and biomolecular systems using BOSS and MCPRO. *J. Comput. Chem.* **2005**, *26*, 1689–1700.

(39) Qiu, Y.; Smith, D. G.; Stern, C. D.; Feng, M.; Jang, H.; Wang, L. P. Driving torsion scans with wavefront propagation. *J. Chem. Phys.* **2020**, *152*, 1–37.

(40) Abraham, M. J.; Murtola, T.; Schulz, R.; Páll, S.; Smith, J. C.; Hess, B.; Lindah, E. Gromacs: High performance molecular simulations through multi-level parallelism from laptops to supercomputers. *SoftwareX* **2015**, *1-2*, 19–25.

(41) Thenmozhi, S.; Subbiahpandi, A.; Dhayalan, V.; Mohanakrishnan, A. K. 1-(Phenylsulfon-yl)benzo[1,2:2,3]thieno[5,4-b] carbazole. *Acta Crystallogr. Sect. E Struct. Reports Online* **2010**, *66*.

(42) Méhes, G.; Goushi, K.; Potscavage, W. J.; Adachi, C. Influence of host matrix on

thermally-activated delayed fluorescence: Effects on emission lifetime, photoluminescence quantum yield, and device performance. *Org. Electron.* **2014**, *15*, 2027–2037.

(43) Bindal, R. D.; Bindal, R. D.; Katzenellenbogen, J. A.; Golab, J. T. Ab Initio Calculations on N-Methylmethanesulfonamide and Methyl Methanesulfonate for the Development of Force Field Torsional Parameters and Their Use in the Conformational Analysis of Some Novel Estrogens. *J. Am. Chem. Soc.* **1990**, *112*, 7861–7868.

(44) Cerezo, J.; Prampolini, G.; Cacelli, I. Developing accurate intramolecular force fields for conjugated systems through explicit coupling terms. *Theor. Chem. Acc.* **2018**, *137*, 1–15.

(45) Smith, J. S.; Isayev, O.; Roitberg, A. E. ANI-1: an extensible neural network potential with DFT accuracy at force field computational cost. *Chem. Sci.* **2017**, *8*, 3192–3203.

(46) Cole, D. J.; Mones, L.; Csányi, G. A machine learning based intramolecular potential for a flexible organic molecule. *Faraday Discuss.* **2020**, *224*, 247–264.

Graphical TOC Entry